

A parametric study on probabilistic fracture of functionally graded composites by a concurrent multiscale method

Arindam Chakraborty, Sharif Rahman *

College of Engineering, The University of Iowa, Iowa City, IA 52242, United States

ARTICLE INFO

Article history:

Received 31 July 2008

Received in revised form

26 December 2008

Accepted 9 January 2009

Available online 21 January 2009

Keywords:

Level-cut

Filtered Poisson field

Random microstructure

Porosity

Stress intensity factors

Fracture toughness

Monte Carlo simulation

Fracture reliability

Crack propagation

ABSTRACT

This article reports the results of a parametric study on the fracture behavior of a crack in functionally graded materials. The study involves stochastic descriptions of particle and void numbers; location, size, and orientation characteristics; and constituent elastic properties; a concurrent multiscale model for calculating crack-driving forces; and Monte Carlo simulation for fracture reliability analysis. A level-cut, inhomogeneous, filtered Poisson field describes the statistically inhomogeneous microstructures of graded composites. Numerical results for an edge-cracked, graded specimen show that the particle shape and orientation for the same phase volume fractions have negligible effects on fracture reliability, even for graded materials with a high modular ratio. However, voids and the particle gradation parameter, if they exist or increase, can significantly raise the probability of fracture initiation. Limited crack-propagation simulations in graded composites containing brittle particles reveal that the fracture toughness of the matrix material can significantly influence the likelihood or the extent of crack growth.

© 2009 Elsevier Ltd. All rights reserved.

1. Introduction

Assessing mechanical reliability of functionally graded materials (FGMs), which possess spatially varying material compositions and microstructures, mandates a fundamental understanding of their deformation and fracture behavior [1,2]. Most existing studies on FGM fracture [3–6] entail calculating crack-driving forces employing smoothly varying material properties that are derived from empirical rules of mixtures, classical bounds, or micromechanical homogenization [7,8]. However, an FGM is a multiphase, heterogeneous material with possibly distinct properties of individual phases. Depending on the crack-tip location and FGM microstructure, the resulting crack-driving forces can be markedly different when a significant mismatch exists in the properties of constituent material phases. Therefore, using homogenized properties in a macroscale analysis may lead to inaccurate or inadequate measures of crack-driving forces and fracture behavior of FGMs. The calculation of crack-driving forces becomes further complicated when accounting for a random microstructure, including spatial and random distributions of sizes, shapes, and orientations of constituent phases [9–12]. Therefore, in general, a

stochastic fracture analysis incorporating random microstructural details, particularly in the crack-tip region, is required for high-fidelity reliability analysis [13].

A valuable insight can be gained by investigating how micromechanical parameters, such as the phase volume fraction, location, size, shape, and orientation of particles; porosity; and the fracture toughness properties of constituents, influence the fracture behavior of a particle-matrix FGM. An elaborate computational model, e.g., a microscale model that employs a discrete particle-matrix system in the entire domain of an FGM, can be invoked for such a parametric study. However, a microscale model, although capable of furnishing highly accurate solutions, constitutes a brute-force approach, and is therefore computationally expensive, if not prohibitive. An attractive alternative is multiscale analysis, where effective material properties are employed whenever possible, thereby solving a fracture problem of interest not only accurately, but also economically. For example, a concurrent multiscale model [13], recently developed by the authors, involves stochastic description of an FGM microstructure and constituent material properties, a two-scale algorithm including microscale and macroscale analyses for determining crack-driving forces, and the Monte Carlo simulation for fracture reliability analysis. Numerical results indicate that the concurrent multiscale model is sufficiently accurate, gives fracture probability solutions very close to those generated from the microscale model, and can reduce the computational effort of the latter model by more than a factor of

* Corresponding address: Department of Mechanical and Industrial Engineering, The University of Iowa, Iowa City 52242, IA, United States. Tel.: +1 319 335 5679; fax: +1 319 335 5669.

E-mail address: rahman@engineering.uiowa.edu (S. Rahman).

two. Therefore, a detailed parametric study can be efficiently conducted using the concurrent multiscale model – the principal focus of this work. In general, the crack-driving forces experienced by an FGM can be very complex in practical scenarios involving a variety of combinations of microstructural parameters and constituent material properties. A clear understanding of the relationship between the microstructure and fracture behavior is vital to the successful application of FGM to the design of mechanical and structural components.

This paper presents the results of a parametric study on fracture behavior of two-dimensional, functionally graded composites. The study involves: (1) stochastic descriptions of particle and void numbers; location, size, and orientation characteristics; and constituent elastic properties; (2) a concurrent multiscale model for determining crack-driving forces under mixed-mode loading; and (3) Monte Carlo simulation for uncertainty propagation and fracture reliability analysis. Section 2 describes a generic fracture problem and a concurrent multiscale model for calculating various fracture response characteristics of interest, defines the random input parameters, and discusses crack-driving forces and fracture reliability. Section 3 describes the Monte Carlo simulation method for calculating statistical moments and probability densities of crack-driving forces, leading to the probability of fracture initiation. A numerical example comprising eight cases of FGM microstructure and three cases of fracture toughness of matrix, and the resultant fracture response, is presented in Section 4. Section 5 provides conclusions from this work and discusses future work.

2. Stochastic fracture mechanics

Consider a three-phase, functionally graded, heterogeneous solid with a rectilinear crack, domain $\mathcal{D} \subset \mathbb{R}^2$, and a schematic illustration of its microstructure, as shown in Fig. 1. The microstructure in general includes three distinct material phases: one phase as particles, another phase as the matrix material, and the remaining phase as voids. The particle, matrix, and void subdomains are represented by \mathcal{D}_p , \mathcal{D}_m , and \mathcal{D}_v , respectively, where $\mathcal{D}_p \cup \mathcal{D}_m \cup \mathcal{D}_v = \mathcal{D}$ and $\mathcal{D}_p \cap \mathcal{D}_m = \mathcal{D}_m \cap \mathcal{D}_v = \mathcal{D}_p \cap \mathcal{D}_v = \emptyset$. A three-phase FGM, henceforth described as a two-phase, porous FGM or simply a porous FGM, can be reduced to a two-phase, non-porous FGM by discarding the void constituent. The particle and matrix represent isotropic and linear-elastic materials, and the elasticity tensors of individual phases, denoted by $\mathbf{C}^{(i)}$, are expressed as [14]

$$\mathbf{C}^{(i)} := \frac{\nu_i E_i}{(1 + \nu_i)(1 - 2\nu_i)} \mathbf{1} \otimes \mathbf{1} + \frac{E_i}{(1 + \nu_i)} \mathbf{I}; \quad i = p, m, \quad (1)$$

where the symbol \otimes denotes the tensor product; E_i and ν_i are the elastic modulus and Poisson's ratio, respectively, of phase i ; and $\mathbf{1}$ and \mathbf{I} are second- and fourth-rank identity tensors, respectively. The superscripts or subscripts $i = p$ and $i = m$ refer to particle and matrix, respectively. At a spatial point $\mathbf{x} \in \mathcal{D}$ in the macroscopic length scale, let $\phi_p(\mathbf{x})$, $\phi_m(\mathbf{x})$, and $\phi_v(\mathbf{x})$ denote the volume fractions of particle, matrix, and void, respectively. Each volume fraction is bounded between 0 and 1 and satisfies the constraint: $\phi_p(\mathbf{x}) + \phi_m(\mathbf{x}) + \phi_v(\mathbf{x}) = 1$. The crack faces are traction-free, and there is perfect bonding between the material phases.

Consider a linear-elastic solid with small displacements and strains. The equilibrium equation and boundary conditions for the quasi-static problem are

$$\nabla \cdot \boldsymbol{\sigma} + \mathbf{b} = \mathbf{0} \text{ in } \mathcal{D}_p \cup \mathcal{D}_m \text{ or } \mathcal{D} \setminus \mathcal{D}_v \quad \text{and} \quad (2)$$

$$\begin{aligned} \boldsymbol{\sigma} \cdot \mathbf{n} &= \bar{\mathbf{t}} \quad \text{on } \Gamma_t \text{ (natural boundary conditions)} \\ \mathbf{u} &= \bar{\mathbf{u}} \quad \text{on } \Gamma_u \text{ (essential boundary conditions),} \end{aligned} \quad (3)$$

respectively, where $\mathbf{u} : \mathcal{D} \rightarrow \mathbb{R}^2$ is the displacement vector; $\boldsymbol{\sigma} = \mathbf{C}(\boldsymbol{\epsilon}) : \boldsymbol{\epsilon}$ is the Cauchy stress tensor with $\mathbf{C}(\boldsymbol{\epsilon})$ and $\boldsymbol{\epsilon} :=$

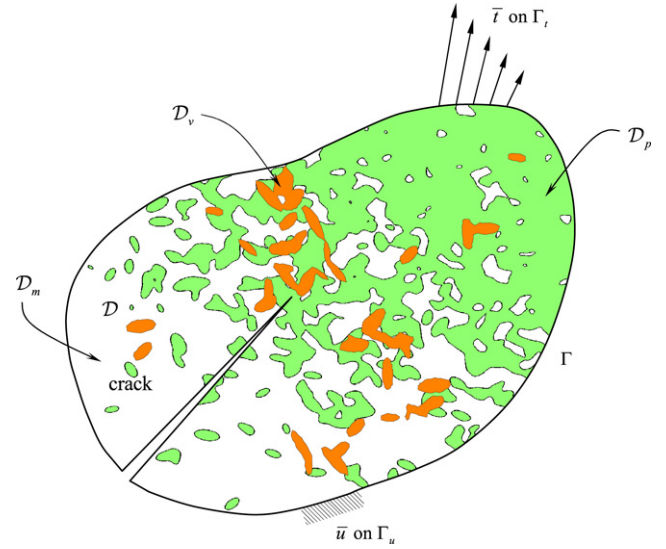


Fig. 1. A crack in a three-phase functionally graded composite. (Note: \mathcal{D} = domain of the entire solid, \mathcal{D}_p = particle subdomain, \mathcal{D}_m = matrix subdomain, \mathcal{D}_v = void subdomain.)

$(1/2)(\nabla + \nabla^T)\mathbf{u}$ denoting the spatially variant elasticity tensor and strain tensor, respectively; \mathbf{n} is a unit outward normal to the boundary Γ of the solid; Γ_t and Γ_u are two disjoint portions of the boundary Γ , where the traction vector $\bar{\mathbf{t}}$ and displacement $\bar{\mathbf{u}}$ are prescribed; $\nabla^T := \{\partial/\partial x_1, \partial/\partial x_2\}$ is the vector of gradient operators; and symbols “ \cdot ” and “ $:$ ” denote dot product and tensor contraction, respectively.

The variational or weak form of Eqs. (2) and (3) is

$$\begin{aligned} \int_{\mathcal{D}} (\mathbf{C}(\boldsymbol{\epsilon}) : \boldsymbol{\epsilon}) : \delta \boldsymbol{\epsilon} d\mathcal{D} - \int_{\mathcal{D}} \mathbf{b} \cdot \delta \mathbf{u} d\mathcal{D} - \int_{\Gamma_t} \bar{\mathbf{t}} \cdot \delta \mathbf{u} d\Gamma \\ - \sum_{\mathbf{x}_K \in \Gamma_u} \mathbf{f}^T(\mathbf{x}_K) \cdot \delta \mathbf{u}(\mathbf{x}_K) - \sum_{\mathbf{x}_K \in \Gamma_u} \delta \mathbf{f}(\mathbf{x}_K) \cdot [\mathbf{u}(\mathbf{x}_K) - \bar{\mathbf{u}}(\mathbf{x}_K)] = 0, \end{aligned} \quad (4)$$

where $\mathbf{f}^T(\mathbf{x}_K)$ is the vector of reaction forces at a constrained node K on Γ_u , and δ denotes the variation operator. The discretization of the weak form, Eq. (4), depends on how the elasticity tensor $\mathbf{C}(\boldsymbol{\epsilon})$ is defined, i.e., how the elastic properties of constituent material phases and their gradation characteristics are described. In the following section, a concurrent multiscale model is described to approximate $\mathbf{C}(\boldsymbol{\epsilon})$. Nonetheless, a numerical method, e.g., the finite-element method (FEM), is generally required to solve the discretized weak form, providing various response fields of interest.

2.1. Concurrent multiscale model

The FGM microstructure in Fig. 1 contains discontinuities in material properties at the interfaces between the matrix and particles. There exist two approaches with respect to defining the material property for fracture analysis of an FGM cracked structure. One approach involves stress analysis using effective material properties, often smooth and continuous, in the entire domain of the solid. This approach is referred to as macroscale analysis. The other approach, referred to as microscale analysis, entails stress analysis that is solely based on the exact but discrete material property information derived from the knowledge of explicit particle locations and their geometry. The concurrent multiscale model employed in this work includes both continuous and discrete material representations and requires a combined micromechanical and macromechanical stress analysis.

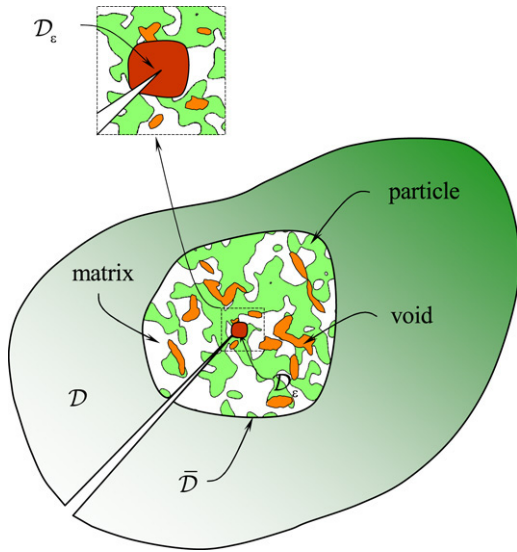


Fig. 2. Schematics of concurrent multiscale model. (Note: \mathcal{D} = domain of the entire solid, $\overline{\mathcal{D}}$ = subdomain with explicit particle and void information, \mathcal{D}_ϵ = small subdomain surrounding crack tip.)

As depicted in Fig. 2, consider an arbitrary bounded subdomain $\overline{\mathcal{D}} \subseteq \mathcal{D}$, which surrounds the crack tip and contains finite numbers of particles and voids. Employing effective elastic properties at the crack-tip region may yield inadequate estimates of the resultant stress intensity factors (SIFs), particularly if there exists a significant mismatch between the matrix and particle properties. However, far from the crack tip, where the effect of crack-tip singularity vanishes rapidly, individual constituent properties may not be needed, and an appropriately derived effective material property should suffice. In other words, the subdomain $\overline{\mathcal{D}}$ is filled with individual particles and voids, whereas the remaining subdomain $\mathcal{D} \setminus \overline{\mathcal{D}}$ is assigned a continuously varying effective elasticity tensor $\mathbf{C}(\mathbf{x})$, derived from a suitable micromechanical homogenization. Using classical micromechanics, e.g., the self-consistent model, the Mori–Tanaka model, and the mean-field theory [7,8], $\overline{\mathbf{C}}(\mathbf{x})$ can be easily calculated from the known phase volume fractions at $\mathbf{x} \in \mathcal{D} \setminus \overline{\mathcal{D}}$. Therefore, according to the concurrent model, Eq. (4) is discretized and solved using [13]

$$\mathbf{C}(\mathbf{x}) \cong \begin{cases} \mathbf{C}^{(p)}, & \text{if } \mathbf{x} \in \overline{\mathcal{D}} \text{ and } \mathbf{x} \in \mathcal{D}_p \\ \mathbf{C}^{(m)}, & \text{if } \mathbf{x} \in \overline{\mathcal{D}} \text{ and } \mathbf{x} \in \mathcal{D}_m \\ \overline{\mathbf{C}}(\mathbf{x}), & \text{if } \mathbf{x} \in \mathcal{D} \setminus \overline{\mathcal{D}}, \end{cases} \quad (5)$$

where discontinuity in material properties exists at the interfaces between $\overline{\mathcal{D}}$ and $\mathcal{D} \setminus \overline{\mathcal{D}}$ and between \mathcal{D}_p and \mathcal{D}_m .

Since the material representation in $\overline{\mathcal{D}}$ is discrete, the calculation of the resulting SIFs in the concurrent model is not straightforward. The interaction integral method, commonly employed for fracture analysis of homogeneous or smoothly inhomogeneous media [3], requires a constant or continuously varying material property inside the domain of a crack-tip contour. However, if a small, bounded, non-porous subdomain $\mathcal{D}_\epsilon \subset \overline{\mathcal{D}} \subseteq \mathcal{D}$ surrounding the crack tip is introduced in slightly modifying the elasticity tensor, for instance [13],

$$\mathbf{C}(\mathbf{x}) \cong \begin{cases} \mathbf{C}^{(p)}, & \text{if } (\mathbf{x} \in \mathcal{D}_\epsilon \text{ and } \mathbf{x}_{\text{tip}} \in \mathcal{D}_p) \text{ or if } (\mathbf{x} \in \overline{\mathcal{D}} \setminus \mathcal{D}_\epsilon \text{ and } \mathbf{x} \in \mathcal{D}_p) \\ \mathbf{C}^{(m)}, & \text{if } (\mathbf{x} \in \mathcal{D}_\epsilon \text{ and } \mathbf{x}_{\text{tip}} \in \mathcal{D}_m) \text{ or if } (\mathbf{x} \in \overline{\mathcal{D}} \setminus \mathcal{D}_\epsilon \text{ and } \mathbf{x} \in \mathcal{D}_m) \\ \overline{\mathbf{C}}(\mathbf{x}), & \text{if } \mathbf{x} \in \mathcal{D} \setminus \overline{\mathcal{D}}, \end{cases} \quad (6)$$

the result is a material representation that is locally homogeneous, i.e., $\mathbf{C}(\mathbf{x})$ is either $\mathbf{C}^{(p)}$ or $\mathbf{C}^{(m)}$, but constant for $\mathbf{x} \in \mathcal{D}_\epsilon$. Therefore, mixed-mode SIFs can be readily calculated from the interaction

integrals applicable to homogeneous materials, provided the crack-tip contour lies inside \mathcal{D}_ϵ . Applying Eq. (6) in solving the discretized weak form yields the interaction integrals, $M_p^{(1,2)}$ and $M_m^{(1,2)}$, when $\mathbf{C}(\mathbf{x}) = \mathbf{C}^{(p)}$; $\mathbf{x} \in \mathcal{D}_\epsilon$ and $\mathbf{C}(\mathbf{x}) = \mathbf{C}^{(m)}$; $\mathbf{x} \in \mathcal{D}_\epsilon$, respectively. The SIFs are subsequently calculated from

$$K_i \cong \begin{cases} \frac{1}{2} M_p^{(1,i)} E_p^*, & \text{if } \mathbf{x}_{\text{tip}} \in \mathcal{D}_p \\ \frac{1}{2} M_m^{(1,i)} E_m^*, & \text{if } \mathbf{x}_{\text{tip}} \in \mathcal{D}_m; \end{cases} \quad i = \text{I, II}, \quad (7)$$

where $E_j^* = E_j$ for the plane stress, $E_j^* = E_j / (1 - \nu_j^2)$ for the plane strain conditions, and $j = p, m$.

In calculating SIFs by the concurrent multiscale model, the size of \mathcal{D}_ϵ should be comparable to the microstructural length scale, but large enough for the SIFs to be calculated accurately. The effects of discrete particles or voids in $\overline{\mathcal{D}}$, if they exist, should be propagated to the SIFs. The magnitude of the effect, however, depends on the size of $\overline{\mathcal{D}}$ relative to \mathcal{D} . Further details of the concurrent model, including verification with a full microscale model, are available in the authors' previous work [13].

2.2. Stochastic input

Uncertainties in FGM fracture analysis leading to stochastic properties of SIFs can come from a variety of sources. Two important sources are: (1) microstructural uncertainty that includes randomness in phase volume fractions, numbers of particles and voids, spatial arrangements of particles and voids, and the size, shape, and orientation properties of particles and voids, and (2) constituent elastic material properties.

2.2.1. Random microstructure

Let (Ω, \mathcal{F}, P) be a probability space, where Ω is the sample space, \mathcal{F} is the σ -algebra of subsets of Ω , and P is the probability measure. Defined on the probability space and indexed by a spatial coordinate $\mathbf{x} \in \mathcal{D} \subset \mathbb{R}^2$, consider an inhomogeneous Poisson random field $\mathcal{N}(\mathcal{D}')$ with an intensity measure $\mu_{\mathcal{D}'} := \int_{\mathcal{D}'} \lambda(\mathbf{x}) d\mathbf{x}$, where $\lambda(\mathbf{x}) \geq 0$ is a spatially variant intensity function associated with the particle or void phase and $\mathcal{D}' \in \mathcal{B}(\mathbb{R}^2)$ is a bounded Borel set such that points of \mathcal{N} falling in $\mathbb{R}^2 \setminus \mathcal{D}'$ do not contribute to particles or voids in \mathcal{D} . The Poisson point field has the following properties: (1) the number $\mathcal{N}(\mathcal{D}')$ of points in a bounded subset \mathcal{D}' has the Poisson distribution with intensity measure $\mu_{\mathcal{D}'}$; and (2) random variables $\mathcal{N}(\mathcal{D}'_1), \dots, \mathcal{N}(\mathcal{D}'_K)$ for any integer $K \geq 2$ and disjoint sets $\mathcal{D}'_1, \dots, \mathcal{D}'_K$ are statistically independent. The Poisson field $\mathcal{N}(\mathcal{D}')$ gives the number of points in \mathcal{D}' and is characterized by the probability

$$P[\mathcal{N}(\mathcal{D}') = n] = \frac{(\int_{\mathcal{D}'} \lambda(\mathbf{x}) d\mathbf{x})^n}{n!} \exp\left(-\int_{\mathcal{D}'} \lambda(\mathbf{x}) d\mathbf{x}\right); \quad n = 0, 1, 2, \dots \quad (8)$$

that n Poisson points exist in \mathcal{D}' . The mean $\mathbb{E}[\mathcal{N}(\mathcal{D}')]$ and variance $\text{Var}[\mathcal{N}(\mathcal{D}')] of $\mathcal{N}(\mathcal{D}')$ are both equal to $\mu_{\mathcal{D}'} := \int_{\mathcal{D}'} \lambda(\mathbf{x}) d\mathbf{x}$.$

Filtered Poisson field: An inhomogeneous, filtered Poisson random field can be described as [9,10]

$$Z(\mathbf{x}) := \begin{cases} 0, & \mathcal{N}(\mathcal{D}') = 0 \\ \sum_{i=1}^{\mathcal{N}(\mathcal{D}')} Z_i h(\Psi_i(\mathbf{x} - \Gamma_i)), & \mathcal{N}(\mathcal{D}') > 0; \end{cases} \quad \mathbf{x} \in \mathcal{D} \subset \mathcal{D}' \subset \mathbb{R}^2, \quad (9)$$

where $\{\Gamma_i\}$ is a collection of Poisson points, $h: \mathbb{R}^2 \rightarrow \mathbb{R}$ is a non-negative kernel function, $\{Z_i\}$ is a collection of independent

and identically distributed real-valued random variables, and $\{\Psi_i\}$ is a collection of independent and identically distributed rotation matrices in \mathbb{R}^2 , for instance,

$$\Psi_i = \begin{bmatrix} \cos \Theta_i & \sin \Theta_i \\ -\sin \Theta_i & \cos \Theta_i \end{bmatrix}; \quad i = 1, \dots, \mathcal{N}; \quad \mathbf{x} \in \mathbb{R}^2, \quad (10)$$

with Θ_i representing deterministic or random orientation of the i th particle or void. In Eq. (9), both \mathcal{D} and \mathcal{D}' are bounded subsets of \mathbb{R}^2 such that points of \mathcal{N} falling in the set difference $\mathbb{R}^2 \setminus \mathcal{D}'$ do not contribute to the value of Z in \mathcal{D} . Also, the subset \mathcal{D}' is bounded if, for example, \tilde{h} has a compact support. The filtered Poisson field $Z(\mathbf{x})$ can be viewed as the response of a filter with a transfer function at point \mathbf{x} that is subjected to a collection of random pulses arriving at Poisson points $\{\Gamma_i\}$.

Level-cut, Filtered Poisson Field: For an increasing function $g : \mathbb{R} \rightarrow \mathbb{R}$, consider a real-valued translation random field

$$Y(\mathbf{x}) := g(Z(\mathbf{x})), \quad (11)$$

which describes a memoryless, measurable, nonlinear function of a real-valued random field $Z(\mathbf{x})$. The translation field $Y(\mathbf{x})$ is completely determined by mapping g and statistical properties of $Z(\mathbf{x})$. Consider a special form of

$$g(z) = I(z; a) := \begin{cases} 1, & z > a \\ 0, & z \leq a; \end{cases} \quad z \in \mathbb{R}, \quad (12)$$

where a is a deterministic constant, known as level, and $I(z; a)$ denotes an indicator function. The translation field Y in Eq. (11) with g in Eq. (12) is referred to as a level-cut random field. By clipping the inhomogeneous, filtered Poisson field $Z(\mathbf{x})$ defined in Eq. (9), the resulting translation field

$$Y(\mathbf{x}) := I(Z(\mathbf{x}); a) \quad (13)$$

then becomes a level-cut, inhomogeneous, filtered Poisson field, which provides a convenient model for a two-phase FGM microstructure in \mathcal{D} . For example, the subsets $\{\mathbf{x} \in \mathcal{D} : Y(\mathbf{x}) = 1\}$ and $\{\mathbf{x} \in \mathcal{D} : Y(\mathbf{x}) = 0\}$ define particles (phase 1) and matrix (phase 2), respectively, which can be derived from the contour of $Z(\mathbf{x})$ at level a . Fig. 3 depicts a schematic illustration of the two subsets, obtained from a cut (Fig. 3(b)) of a generic random field $Z(\mathbf{x})$ (Fig. 3(a)). The dark (charcoal) phase indicates particles embedded in the light (light blue) phase representing the matrix. The level-cut random field can also be employed for modeling porosity (void) in the matrix.

Approximate level-cut, filtered Poisson field: Let the kernel $\tilde{h}(\chi)$ be a compactly supported, non-negative function, for example,

$$\tilde{h}(\chi) = \begin{cases} \exp(-\chi^\top \boldsymbol{\gamma} \chi) = \exp\left(-\frac{\chi_1^2}{\sigma_1^2} - \frac{\chi_2^2}{\sigma_2^2}\right), & \text{for particles} \\ \chi^\top \boldsymbol{\gamma} \chi = \frac{\chi_1^2}{\sigma_1^2} + \frac{\chi_2^2}{\sigma_2^2}, & \text{for voids,} \end{cases} \quad (14)$$

where $\chi \in \mathbb{R}^2$, $\sigma_k > 0$ are some constants, and $\boldsymbol{\gamma} = \text{diag}[1/\sigma_1, 1/\sigma_2] \in \mathbb{R}^{2 \times 2}$ is a diagonal matrix. Suppose that $\lambda(\mathbf{x})$, Z_i , and \tilde{h} are such that the values of Z in a small vicinity $\mathcal{D}(\Gamma_i)$ of Γ_i can be approximated by

$$\tilde{Z}(\mathbf{x}) = Z_i \tilde{h}(\Psi_i(\mathbf{x} - \Gamma_i)), \quad \mathbf{x} \in \mathcal{D}(\Gamma_i), \quad (15)$$

leading to an approximate version

$$\tilde{Y}(\mathbf{x}) = I(\tilde{Z}(\mathbf{x}); a) = I(Z_i \tilde{h}(\Psi_i(\mathbf{x} - \Gamma_i)); a), \quad \mathbf{x} \in \mathcal{D}(\Gamma_i) \quad (16)$$

of the level-cut field $Y(\mathbf{x})$ in Eq. (13). Therefore, the particles or voids in the microstructure of a two-phase FGM can be conveniently approximated by the subsets

$$\begin{aligned} (\mathbf{x} - \Gamma_i)^\top \Psi_i^\top \boldsymbol{\gamma} (\mathbf{x} - \Gamma_i) &\leq -\ln(a/Z_i), & \text{for particles} \\ (\mathbf{x} - \Gamma_i)^\top \Psi_i^\top \boldsymbol{\gamma} (\mathbf{x} - \Gamma_i) &= 1, & \text{for voids,} \end{aligned} \quad (17)$$

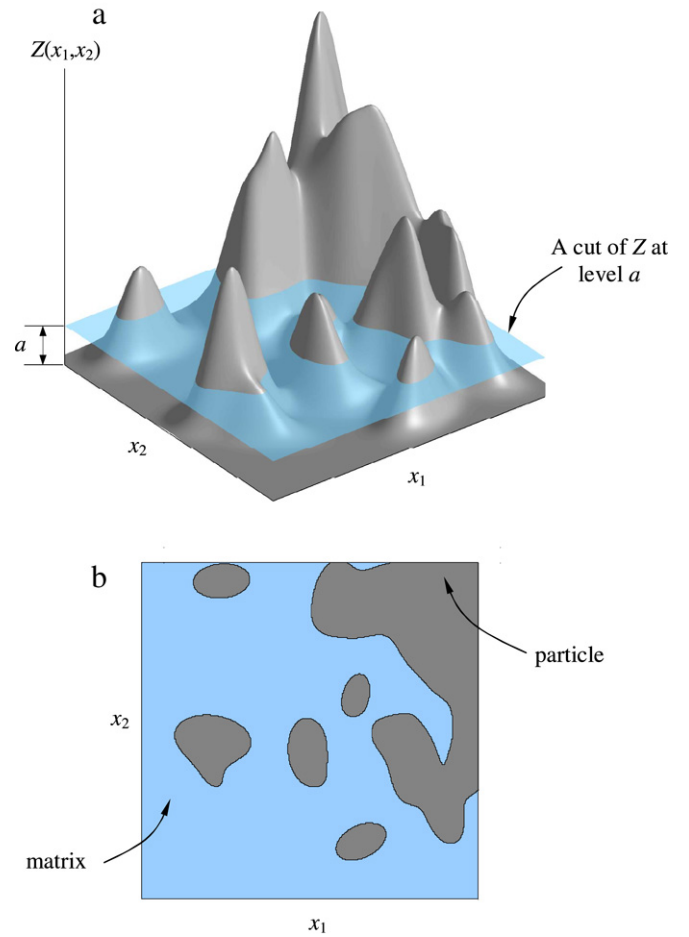


Fig. 3. Schematic illustration of a generic level-cut random field in \mathbb{R}^2 ; (a) a sample of $Z(x_1, x_2)$ with a cut at level a ; (b) two subsets of $Y(x_1, x_2)$ obtained from the contour of the sample of $Z(x_1, x_2)$ at level a .

of \mathcal{D} for $Z_i > a$ and $\mathbf{x} \in \mathbb{R}^2$. The approximate level-cut field is capable of generating particles and voids with regular geometric shapes, e.g., circular, elliptical. Note that $\tilde{Y}(\mathbf{x})$ is strictly applicable when $\lambda(\mathbf{x})$ and σ_k are both small. While such smallness restriction limits the usefulness of $\tilde{Y}(\mathbf{x})$ somewhat, Eqs. (16) and (17) can be conveniently employed for finite-element discretization of fully penetrable particles even when $\lambda(\mathbf{x})$ and σ_k are not small. See Rahman [10] for further details.

Algorithm: The level-cut field $\tilde{Y}(\mathbf{x})$, described by Eq. (16), can be obtained from $\tilde{Z}(\mathbf{x})$ using the level-cut parameter a . Once all the parameters of the level-cut field $\tilde{Y}(\mathbf{x})$ have been determined, samples of synthetic microstructures of two-phase FGMs can be generated based on the following algorithm:

- Step 1: Define bounded subsets \mathcal{D} and \mathcal{D}' of \mathbb{R}^2 . The bounded subset \mathcal{D}' must be such that points of \mathcal{N} falling in $\mathbb{R}^2 \setminus \mathcal{D}'$ do not contribute to the value of $\tilde{Z}(\mathbf{x})$ in \mathcal{D} . Specify the kernel function \tilde{h} and define its parameters.
- Step 2: Generate a sample k^* of the homogeneous Poisson random variable $N^*(\mathcal{D}')$, which has a constant intensity $\lambda^* = \max_{\mathbf{x} \in \mathbb{R}^2} \lambda(\mathbf{x})$, where $\lambda(\mathbf{x})$ is a bounded intensity function in \mathcal{D}' .
- Step 3: Generate k^* independent uniformly distributed points in \mathcal{D}' . Denote these points by \mathbf{x}_i , $i = 1, \dots, k^*$.
- Step 4: Perform thinning of the point set obtained in Step 3. In so doing, each point \mathbf{x}_i , independently of the other, is kept with probability $\lambda(\mathbf{x}_i)/\lambda^*$, which is equivalent to discarding the point with probability $1 - \lambda(\mathbf{x}_i)/\lambda^*$. The resulting point pattern

with the size $k^{**} \leq k^*$ follows the inhomogeneous Poisson field $\mathcal{N}(\mathcal{D}')$ with intensity function $\lambda(\mathbf{x})$. Denote these points by Γ_i , $i = 1, \dots, k^{**}$.

- Step 5: Generate k^{**} independent samples of random rotation matrices $\{\Psi_i\}$ and random variables $\{Z_i\}$ from their relevant distributions.
- Step 6: Calculate the corresponding samples of the random fields $\tilde{Z}(\mathbf{x})$ from Eq. (15) and $\tilde{Y}(\mathbf{x})$ from Eq. (16) for a specified level a . The sample of $\tilde{Y}(\mathbf{x})$ yields a two-phase, statistically inhomogeneous microstructure in \mathcal{D} .

Independent samples of $\tilde{Z}(\mathbf{x})$ and $\tilde{Y}(\mathbf{x})$ are delivered by repeated application of the above-stated algorithm.

Different functions and parameters involved in generating the level-cut field $\tilde{Y}(\mathbf{x})$ are: (1) a Poisson field $\mathcal{N}(\mathcal{D}')$ that gives the number of points in \mathcal{D}' , (2) a spatially variant intensity function $\lambda(\mathbf{x})$ that is related to particle or void volume fraction, (3) random variables $\{Z_i\}$ that are related to random particle or void sizes, (4) a non-negative kernel function h , which determines particle or void shape (e.g., elliptical particles using $\sigma_1 \neq \sigma_2$), (5) random rotation matrices $\{\Psi_i\}$ that determine particle or void orientations, and (6) a variable a denoting the level at which the cut is made, affecting also the size of particle or void. In the present study, $\lambda(\mathbf{x})$ as well as the non-negative kernel function h and the level-cut variable a are deterministic. The use of deterministic intensity function makes the phase volume fraction deterministic.

The level-cut, inhomogeneous, filtered Poisson random field and the associated algorithm for microstructures described in the preceding pertain to any two-phase FGM. Therefore microstructures of a non-porous, particle-matrix FGM can be readily generated. For a porous, particle-matrix FGM, the microstructures can be delivered by a three-step serial process: (1) generate a two-phase, non-porous, particle-matrix FGM microstructure; (2) generate a two-phase, void-matrix FGM microstructure; and (3) superimpose the microstructure from Step 2 over that from Step 1, forming a resultant microstructure of a porous, particle-matrix FGM. The resultant microstructure includes particles, voids, and matrix as constituents.

2.2.2. Random constituent elastic properties

In addition to a random microstructure, the constituent elastic (isotropic) properties of material phases can be stochastic, as assumed in the present study. Let E_p and ν_p denote the elastic modulus and Poisson's ratio, respectively, of the particle, and E_m and ν_m denote the elastic modulus and Poisson's ratio, respectively, of the matrix. Therefore, the random vector $\{E_p, E_m, \nu_p, \nu_m\}^T \in \mathbb{R}^4$ describes the stochastic elastic properties of both constituents. The constituent properties are spatially invariant in the macroscopic length scale.

2.2.3. Input random vector

Let $\lambda_p(\mathbf{x})$ or $\lambda_v(\mathbf{x})$ denote intensity functions associated with the particle or void, respectively, in \mathcal{D} . Using these intensity functions, let the Poisson random variables $\overline{\mathcal{N}}_p$ and $\overline{\mathcal{N}}_v$ represent the number of particles and voids, respectively, in $\overline{\mathcal{D}'}$, where $\overline{\mathcal{D}'} \subset \mathbb{R}^2$ is a bounded subset such that points of $\overline{\mathcal{N}}_p$ and $\overline{\mathcal{N}}_v$ falling in $\overline{\mathcal{D}'} \setminus \overline{\mathcal{D}'}$ do not contribute to particles and voids, respectively, in $\overline{\mathcal{D}'}$. Denote the coordinates of the centroids of particles and voids by $U_{p_i,1}, U_{p_i,2}; i = 1, \dots, \overline{\mathcal{N}}_p$ and $U_{v_i,1}, U_{v_i,2}; i = 1, \dots, \overline{\mathcal{N}}_v$ respectively. Correspondingly, the random scaling variables and orientations are: Z_{p_i} and $\Theta_{p_i}; i = 1, \dots, \overline{\mathcal{N}}_p$ for particles; and Z_{v_i} and $\Theta_{v_i}; i = 1, \dots, \overline{\mathcal{N}}_v$ for voids. Table 1 lists all stochastic input variables for both non-porous and porous FGMs. Let $\mathbf{R} \in \mathbb{R}^N$ denote an N -dimensional input random vector that contains uncertainties from all sources described in Sections 2.2.1 and 2.2.2. Therefore, the

total number (N) of random variables is $4\overline{\mathcal{N}}_p + 5$ for non-porous FGM and $4\overline{\mathcal{N}}_p + 4\overline{\mathcal{N}}_v + 6$ for porous FGM. The input random vector \mathbf{R} characterizes uncertainties from all sources in an FGM and is completely described by its joint probability density function $f_{\mathbf{R}}(\mathbf{r})$, where \mathbf{r} is a realization of \mathbf{R} .

2.3. Crack-driving forces and reliability

A major objective of stochastic fracture-mechanics analysis is to find probabilistic characteristics of crack-driving forces, such as SIFs $K_I(\mathbf{R})$ and $K_{II}(\mathbf{R})$ for modes I and II, respectively, and the J -integral and other fracture integrals, due to uncertain input \mathbf{R} . For a given input, the standard FEM can be employed to solve the discretized weak form (Eq. (4)), leading to the calculation of SIFs and other crack-driving forces.

Suppose that failure is defined when the crack propagation is initiated at a crack tip, i.e., when $K_{\text{eff}}(\mathbf{R}) = h(K_I(\mathbf{R}), K_{II}(\mathbf{R})) > K_{Ic}$, where K_{eff} is an effective SIF with h depending on a selected mixed-mode theory, and K_{Ic} is a relevant mode-I fracture toughness of the material measured in terms of SIF. This requirement cannot be satisfied with certainty, since K_I and K_{II} are both dependent on \mathbf{R} , which is random, and K_{Ic} itself may be a random variable or field. Hence, the performance of a cracked FGM should be evaluated by the conditional reliability or its complement, the conditional probability of failure P_F , defined as the multifold integral

$$P_F(K_{Ic}) := P[y(\mathbf{R}) < 0] := \int_{\mathbb{R}^N} \mathbb{I}_y(\mathbf{r}) f_{\mathbf{R}}(\mathbf{r}) \, d\mathbf{r}, \quad (18)$$

where

$$y(\mathbf{R}) = K_{Ic} - h(K_I(\mathbf{R}), K_{II}(\mathbf{R})) \quad (19)$$

is a multivariate performance function that depends on the random input \mathbf{R} and

$$\mathbb{I}_y(\mathbf{r}) = \begin{cases} 1, & \text{if } y(\mathbf{r}) < 0 \\ 0, & \text{if } y(\mathbf{r}) > 0 \end{cases} \quad (20)$$

is another indicator function. In this work, the maximum circumferential stress theory was invoked to describe mixed-mode fracture initiation [15].

The evaluation of the multidimensional integral in Eq. (18), either analytically or numerically, is not possible because the total number of random variables N is large, $f_{\mathbf{R}}(\mathbf{r})$ is generally non-Gaussian, and $y(\mathbf{r})$ is a highly nonlinear function of \mathbf{r} . Therefore, Monte Carlo simulation was employed for calculating the probabilistic characteristics of crack-driving forces and the probability of fracture initiation.

3. Monte Carlo simulation

Recall that $K_i(\mathbf{r}) = K_i(r_1, \dots, r_N); i = \text{I, II}$ and $y(\mathbf{r}) = y(r_1, \dots, r_N)$ represent crack-driving forces or a performance function that depends on crack-driving forces. The number of input random variables N , the dimension of the stochastic problem, and the input-output mapping $K_i : \mathbb{R}^N \rightarrow \mathbb{R}$ or $y : \mathbb{R}^N \rightarrow \mathbb{R}$ depends on the concurrent multiscale model. The objective is to evaluate the probabilistic characteristics of generic output responses $K_i(\mathbf{R})$ or $y(\mathbf{R})$, when the probability distribution of the random input $\mathbf{R} \in \mathbb{R}^N$ is prescribed.

Consider a generic N -dimensional random vector $\mathbf{R} = \{R_1, \dots, R_N\}^T$, which characterizes uncertainty in all input parameters under consideration with its known joint PDF $f_{\mathbf{R}}(\mathbf{r})$. Suppose that $\mathbf{r}^{(1)}, \dots, \mathbf{r}^{(L)}$ are L realizations of the input vector \mathbf{R} , which can be generated independently. Let $K_i(\mathbf{r}^{(1)}), \dots, K_i(\mathbf{r}^{(L)}); i = \text{I, II}$ and $y(\mathbf{r}^{(1)}), \dots, y(\mathbf{r}^{(L)})$ be the output samples of mixed-mode SIFs

Table 1
List of stochastic inputs.

	Two-phase FGM (non-porous)	Three-phase FGM (porous)
Microstructural parameters	$\overline{\mathcal{N}}_p^a$ $(U_{p_{i,1}}, U_{p_{i,2}}); i = 1, \dots, \overline{\mathcal{N}}_p$ $Z_{p_i}; i = 1, \dots, \overline{\mathcal{N}}_p$ $\Theta_{p_i}; i = 1, \dots, \overline{\mathcal{N}}_p$	$\overline{\mathcal{N}}_p, \overline{\mathcal{N}}_v^b$ $(U_{p_{i,1}}, U_{p_{i,2}}); i = 1, \dots, \overline{\mathcal{N}}_p$ $(U_{v_{i,1}}, U_{v_{i,2}}); i = 1, \dots, \overline{\mathcal{N}}_v$ $Z_{p_i}; i = 1, \dots, \overline{\mathcal{N}}_p$ $Z_{v_i}; i = 1, \dots, \overline{\mathcal{N}}_v$ $\Theta_{p_i}; i = 1, \dots, \overline{\mathcal{N}}_p$ $\Theta_{v_i}; i = 1, \dots, \overline{\mathcal{N}}_v$
Constituent properties	E_p, E_m, ν_p, ν_m	E_p, E_m, ν_p, ν_m
Input random vector (\mathbf{R})	$\{\overline{\mathcal{N}}_p, (U_{p_{1,1}}, U_{p_{1,2}}), \dots, (U_{p_{\overline{\mathcal{N}}_p,1}}, U_{p_{\overline{\mathcal{N}}_p,2}}), Z_{p_1}, \dots, Z_{p_{\overline{\mathcal{N}}_p}}, \Theta_{p_1}, \dots, \Theta_{p_{\overline{\mathcal{N}}_p}}, E_p, E_m, \nu_p, \nu_m\}^T \in \mathbb{R}^N$	$\{\overline{\mathcal{N}}_p, (U_{p_{1,1}}, U_{p_{1,2}}), \dots, (U_{p_{\overline{\mathcal{N}}_p,1}}, U_{p_{\overline{\mathcal{N}}_p,2}}), Z_{p_1}, \dots, Z_{p_{\overline{\mathcal{N}}_p}}, \Theta_{p_1}, \dots, \Theta_{p_{\overline{\mathcal{N}}_p}}, \overline{\mathcal{N}}_v, (U_{v_{1,1}}, U_{v_{1,2}}), \dots, (U_{v_{\overline{\mathcal{N}}_v,1}}, U_{v_{\overline{\mathcal{N}}_v,2}}), Z_{v_1}, \dots, Z_{v_{\overline{\mathcal{N}}_v}}, \Theta_{v_1}, \dots, \Theta_{v_{\overline{\mathcal{N}}_v}}, E_p, E_m, \nu_p, \nu_m\}^T \in \mathbb{R}^N$
Total number of random variables (N)	$4\overline{\mathcal{N}}_p + 5$	$4\overline{\mathcal{N}}_p + 4\overline{\mathcal{N}}_v + 6$

^a $\overline{\mathcal{N}}_p = \overline{\mathcal{N}}_p(\overline{\mathcal{D}})$, where $\overline{\mathcal{N}}_p$ is a Poisson random variable with intensity function $\lambda_p(\mathbf{x})$.
^b $\overline{\mathcal{N}}_v = \overline{\mathcal{N}}_v(\overline{\mathcal{D}})$, where $\overline{\mathcal{N}}_v$ is a Poisson random variable with intensity function $\lambda_v(\mathbf{x})$.

$K_i(\mathbf{R})$ and performance function $y(\mathbf{R})$ that correspond to the input $\mathbf{r}^{(1)}, \dots, \mathbf{r}^{(L)}$, which can be obtained from repeated deterministic fracture-mechanics evaluations of K_i and y . The l th moment of $K_i(\mathbf{R})$, estimated by Monte Carlo simulation [16] is

$$\mathbb{E}[K_i^l(\mathbf{R})] = \lim_{L \rightarrow \infty} \frac{1}{L} \sum_{j=1}^L [K_i^l(\mathbf{r}^{(j)})], \quad i = \text{I, II.} \quad (21)$$

By setting $l = 1$ and 2 , the mean and standard deviation of $K_i(\mathbf{R})$ and $K_{II}(\mathbf{R})$ can be obtained.

For reliability analysis, the direct Monte Carlo estimate $P_{F,MCS}$ of the conditional failure probability is

$$P_{F,MCS}(K_{Ic}) = \lim_{L \rightarrow \infty} \frac{1}{L} \sum_{j=1}^L [\mathbb{I}_y(\mathbf{r}^{(j)})], \quad (22)$$

where $\mathbb{I}_y(\mathbf{r}^{(j)})$ denotes the j th realization of the indicator function defined in Eq. (20).

4. An edge-cracked FGM specimen

Consider a two-dimensional, square, FGM specimen with domain $\mathcal{D} = 10 \text{ cm} \times 10 \text{ cm}$, which contains randomly dispersed, fully penetrable, elliptical, silicon carbide (SiC) particles and circular voids in an aluminum (Al) matrix. Fig. 4 illustrates a microstructural sample of the specimen, which was created by the level-cut, filtered, random field $\tilde{Y}(\mathbf{x})$ over $\mathcal{D}' = 10.5 \text{ cm} \times 10.5 \text{ cm}$ and random orientations of the particles. The center of \mathcal{D}' coincides with that of \mathcal{D} . The specimen contains a horizontally placed, $a_c = 5 \text{ cm}$ long edge crack with the crack-tip location $\mathbf{x}_{\text{tip}} = \{x_{\text{tip},1}, x_{\text{tip},2}\}^T = \{5, 5\}^T \text{ cm}$ and is subjected to a far-field tensile stress σ^∞ and a far-field shear stress τ^∞ . For stationary crack: $\sigma^\infty = \tau^\infty = 1 \text{ kN/cm}^2$, and for crack propagation: $\sigma^\infty = \tau^\infty = 1.8 \text{ kN/cm}^2$. The subdomains $\overline{\mathcal{D}}$ and $\overline{\mathcal{D}'}$ are $5 \text{ cm} \times 5 \text{ cm}$ and $5.5 \text{ cm} \times 5.5 \text{ cm}$ squares with the center coinciding with the crack tip. The subdomain \mathcal{D}_ϵ is a circle with radius equal to half of the radius of a circle with an area equal to that of the average particle area in $\overline{\mathcal{D}}$. The center of \mathcal{D}_ϵ is located at the crack tip. The sizes of the subdomains $\overline{\mathcal{D}}$ and \mathcal{D}_ϵ are deemed adequate based on the results of the authors' previous study [13]. A plane strain condition was assumed.

4.1. Inputs

Particles and voids were generated using the level-cut, inhomogeneous, filtered Poisson random field $\tilde{Y}(\mathbf{x})$ described in Section 2.2.1. The aspect ratio, defining the length-to-width ratio of

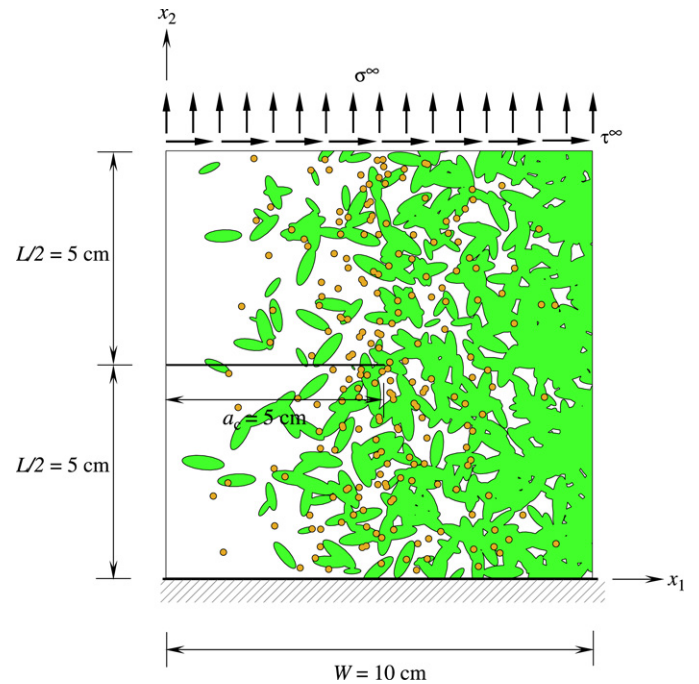


Fig. 4. A porous FGM specimen with an edge crack under a mixed-mode deformation.

each particle or void, and hence the shape, whether elliptical or circular, is deterministic and identical for all particles in a particular sample. The particles and voids both follow horizontally varying Poisson intensity functions

$$\lambda_p(\mathbf{x}) = c_p \ln \frac{1 + \epsilon}{1 + \epsilon - \left(\frac{x_1}{10.5}\right)^{n_p}} \quad (23)$$

and

$$\lambda_v(\mathbf{x}) = \begin{cases} c_v \ln \frac{5.25(1 + \epsilon)}{5.25(1 + \epsilon) - x_1}, & x_1 \leq 5.25 \\ c_v \ln \frac{5.25(1 + \epsilon)}{5.25(1 + \epsilon) - (10.5 - x_1)}, & x_1 > 5.25, \end{cases} \quad (24)$$

respectively, where $\mathbf{x} = \{x_1, x_2\}^T \in \mathbb{R}^2, 0 \leq x_i \leq 10.5 \text{ cm}; i = 1, 2; \epsilon = 10^{-6}; n_p$ is an exponent representing particle gradation; $c_p = 6 \text{ cm}^{-2}$ is the intensity parameter for particles; and c_v is the intensity parameter for voids. The intensity parameters and the corresponding volume fractions ($\phi_i(\mathbf{x})$, say) are related via

Table 2
Statistical properties of constituents in SiC–Al FGM.

Elastic property ^a	Mean	Coefficient of variation (%)	Probability distribution
E_{SiC} (GPa)	419.2	15	Lognormal
E_{Al} (GPa)	69.7	10	Lognormal
ν_{SiC}	0.19	15	Lognormal
ν_{Al}	0.34	10	Lognormal

^a $E_p = E_{SiC}$; $E_m = E_{Al}$; $\nu_p = \nu_{SiC}$; $\nu_m = \nu_{Al}$.

$\phi_i(\mathbf{x}) \cong \mathbb{E}[\tilde{Y}_i(\mathbf{x})] = P[\tilde{Z}_i(\mathbf{x}) > a]$ [9,10]; $i = p, v$, denoting particle and void phases, where the expectation of $\tilde{Y}_i(\mathbf{x})$ and the probability of $\tilde{Z}_i(\mathbf{x})$ both depend on the intensity functions expressed by Eqs. (23) and (24) and hence, on the intensity parameters. Three values of $n_p = 0.5, 1$, and 2 were examined. For voids, three values of c_v were selected: (1) $c_v = 0$, representing non-porous FGM; (2) $c_v = 2.52 \text{ cm}^{-2}$, yielding a void volume fraction of nearly 0.1 at the crack tip; and (3) $c_v = 5.46 \text{ cm}^{-2}$, leading to a void volume fraction of nearly 0.2 at the crack tip. The exponential kernel function for particles is given by Eq. (14), where $\sigma_1 = 0.3 \text{ cm}$; $\sigma_2 = 0.1 \text{ cm}$ for elliptical particles and $\sigma_1 = \sigma_2 = \sqrt{0.3 \times 0.1} \text{ cm}$ for circular particles. A cylindrical kernel function, also represented by Eq. (14), was used for voids, all of which are equal-size circles with $\sigma_1 = \sigma_2 = \sqrt{0.1 \times \text{average particle area}/\pi} \text{ cm}$. The random variables $Z_{p_i} = 10|U_i|$; $i = 1, \dots, \bar{N}_p$ and $Z_{v_i} = 10|U_i|$; $i = 1, \dots, \bar{N}_v$, where $\{U_i\}$ is a collection of independent, standard Gaussian random variables. The orientation of the i th elliptical particle is either random (e.g., $\Theta_{p_i} = U(0, 2\pi)$), i.e., uniformly distributed between 0 and 2π or deterministic (e.g., $\Theta_{p_i} = 0$ or $\pi/2$).

Finally, the material phases SiC and Al are both linear-elastic and isotropic. However, the elastic moduli E_{SiC} and E_{Al} and the Poisson's ratios ν_{SiC} and ν_{Al} , of SiC and Al, respectively, are random variables; their means, standard deviations, and probability distributions are listed in Table 2. The lognormal distribution of the elastic properties, although chosen arbitrarily in this work, was restricted to small coefficients of variation. Therefore, a lognormal or similar other distributions of the elastic properties should reveal the influence of microstructure, if any, on a fracture response of interest. The mode-I fracture toughnesses of SiC and Al, which are deterministic, are as follows: $K_{Ic,SiC} = 5 \text{ MPa}\sqrt{\text{m}}$ and $K_{Ic,Al} = 20, 30$, and $40 \text{ MPa}\sqrt{\text{m}}$. Therefore, the matrix is relatively more ductile than the particles.

4.2. Parameters studied

Four microstructural features and the fracture toughness of Al were considered for a parametric study on fracture behavior of FGMs. They include: (1) particle shape parameters described by σ_1 and σ_2 in Eq. (14); (2) particle orientation represented by Θ_{p_i} (i.e., Θ_i for particles in Eq. (10)); (3) porosity quantified by c_v in Eq. (24); (4) particle gradation characterized by n_p in Eq. (23) and (5) porousfgm mode-I fracture toughness $K_{Ic,Al}$ of Al (matrix). Table 3 summarizes these five parameters, leading to eleven distinct cases for the parametric study. The cases 1–8 account for the effect of FGM microstructural features on the mixed-mode SIFs, leading to fracture initiation. Therefore, they do not include $K_{Ic,Al}$ as it relates to crack propagation, examined in cases 9–11.

Fig. 5(a)–(c) present spatial distributions of particle and void volume fractions for both non-porous and porous FGMs. The volume fractions, $\phi_i(\mathbf{x}) \cong \mathbb{E}[\tilde{Y}_i(\mathbf{x})]$, were calculated from ten independent microstructural samples of $\tilde{Y}_i(\mathbf{x})$, generated using the algorithm in Section 2.2.1. Fig. 5(a) comprises plots of particle volume fractions for four non-porous FGMs with $n_p = 1$: one with

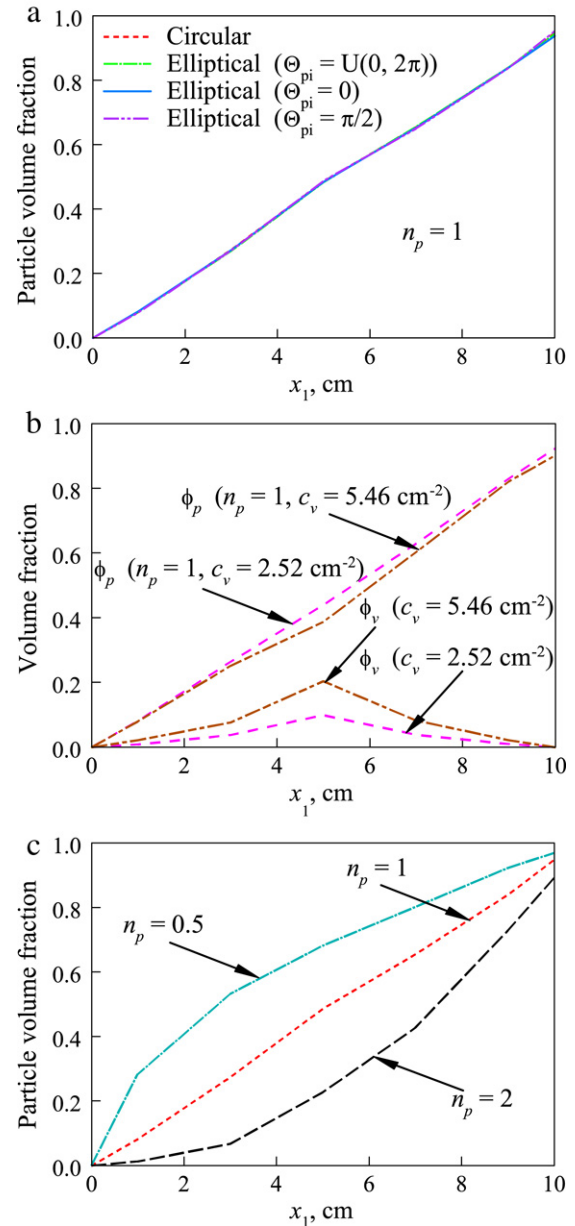


Fig. 5. Phase volume fractions of FGMs: (a) particle volume fractions of non-porous FGMs with different particle shapes and orientations; (b) particle and void volume fractions of porous FGMs; (c) particle volume fractions of non-porous FGMs with different gradations of intensity function.

circular ($\sigma_1 = \sigma_2 = \sqrt{0.3 \times 0.1} \text{ cm}$) particles (case 1) and three with elliptical ($\sigma_1 = 0.3 \text{ cm}$, $\sigma_2 = 0.1 \text{ cm}$) particles entailing $\Theta_{p_i} = U(0, 2\pi)$ (case 2), 0 (case 3), and $\pi/2$ (case 4). All four distributions of particle volume fractions from Fig. 5(a) are practically coincident. Therefore, the individual effects of particle shape and orientation on FGM fracture response can be evaluated. Similarly, Fig. 5(b) shows distributions of particle and void volume fractions for two porous FGMs with $n_p = 1$, obtained by selecting $c_v = 2.52 \text{ cm}^{-2}$ (case 5) and $c_v = 5.46 \text{ cm}^{-2}$ (case 6) (cases 5 and 6). From Fig. 5(b), the maximum void volume fractions that occur at $x_1 = 5 \text{ cm}$ are nearly 0.1 and 0.2, respectively. Finally, Fig. 5(c) depicts three markedly different distributions of particle volume fractions for non-porous FGMs, when the particle gradation parameters are $n_p = 0.5$ (case 7), 1 (case 1), and 2 (case 8). Therefore, n_p controls the spatial distribution of particle volume fractions significantly.

Table 3
Parameters studied and associated cases.

Case	Shape ($\sigma_1, \sigma_2, \text{cm}$)	Orientation (ϕ_p)	Porosity (c_v, cm^{-2})	Particle gradation (n_p)	Fracture toughness of Al ($K_{Ic,Al}, \text{MPa}\sqrt{\text{m}}$)
1	$\sigma_1 = \sigma_2 = \sqrt{0.3 \times 0.1}$	NA ^a	0	1	NA ^a
2	$\sigma_1 = 0.3; \sigma_2 = 0.1$	$U(0, 2\pi)$ ^b	0	1	NA ^a
3	$\sigma_1 = 0.3; \sigma_2 = 0.1$	0	0	1	NA ^a
4	$\sigma_1 = 0.3; \sigma_2 = 0.1$	$\pi/2$	0	1	NA ^a
5	$\sigma_1 = \sigma_2 = \sqrt{0.3 \times 0.1}$	NA ^a	2.52	1	NA ^a
6	$\sigma_1 = \sigma_2 = \sqrt{0.3 \times 0.1}$	NA ^a	5.46	1	NA ^a
7	$\sigma_1 = \sigma_2 = \sqrt{0.3 \times 0.1}$	NA ^a	0	0.5	NA ^a
8	$\sigma_1 = \sigma_2 = \sqrt{0.3 \times 0.1}$	NA ^a	0	2	NA ^a
9	$\sigma_1 = \sigma_2 = \sqrt{0.3 \times 0.1}$	NA ^a	0	1	20
10	$\sigma_1 = \sigma_2 = \sqrt{0.3 \times 0.1}$	NA ^a	0	1	40
11	$\sigma_1 = \sigma_2 = \sqrt{0.3 \times 0.1}$	NA ^a	0	1	30

^a Not applicable.

^b Uniformly distributed between 0 and 2π .

4.3. Finite element modeling

Fig. 6(a)–(h) present eight finite-element discretizations of samples of non-porous and porous FGM specimens for the first eight cases listed in Table 3, all employed in conjunction with the concurrent multiscale model.⁰ The numbers and types of elements for these eight finite-element meshes are listed in Table 4. All finite-element meshes are conforming and were developed using the commercial code ABAQUS [17]. Full 3×3 and 3-point Gauss quadrature rules were employed for the quadrilateral and triangular elements, respectively, for numerical integration.

For finite-element models of porosity, a void falling anywhere on the crack was redistributed in the x_2 direction by splitting the void into two equivalent parts and placing them just above and just below the crack line in such a way that the equivalent voids do not intersect with the crack. Also, since \mathcal{D}_ϵ is non-porous and voids are small compared with particle sizes, any portion of a void falling inside \mathcal{D}_ϵ was ignored and was replaced by the particle or the matrix phase depending on the crack-tip material of the underlying particle-matrix microstructure of the non-porous FGM.

The stochastic analysis was conducted by the Monte Carlo simulation with a sample size of 10,000. Therefore, the smallest value of the failure probability calculated was limited to 10^{-3} . A failure probability of 10^{-3} , although not a very small number, was deemed adequate to conduct the parametric study.

4.4. Results and discussions

Fig. 7(a)–(h) plot von Mises stress contours generated using the concurrent multiscale model for the six non-porous (cases 1, 2, 3, 4, 7, and 8) and two porous (cases 5 and 6) FGM samples in Fig. 6(a)–(h). The effective elastic properties required by the concurrent multiscale model were calculated using the Mori-Tanaka approximation [18], which incorporates orthotropic effective elastic properties due to the alignment of elliptical particles in a particular direction and the aspect ratio. Voids are represented using degenerative material properties in the Mori-Tanaka approximation. The overall stress responses for different FGM samples, indicated by the contour patterns, are similar. However, there are also differences in the local stress fields that may have significant implications in determining crack-driving forces and eventually in statistical and reliability predictions for different microstructures. The second-moment characteristics and fracture reliability results pertaining to parametric study are presented next.

⁰ Finite element discretizations of FGM specimens for cases 9, 10, and 11 are same as that for case 1.

4.4.1. Second-moment statistics of SIFs

Table 5 lists the means and coefficients of variations of K_I and K_{II} for six non-porous FGMs (cases 1, 2, 3, 4, 7, and 8) and two porous FGMs (cases 5 and 6) described in Fig. 6(a)–(h). The results for the mean values of K_I for cases 2–4 are comparable with that for case 1, with a maximum of 3.5% difference observed in case 3. The variability in the K_I values for cases 1–4, expressed in terms of coefficient of variation, shows a similar trend. These results indicate that the statistical properties of mode I SIF do not alter appreciably due to particle shape or orientation. However, the amount of porosity (cases 5 and 6) enhances mode I SIF, as Table 5 shows an increase of 17.6% in the mean value of K_I from case 1 to case 6. However, an introduction of voids does not increase the coefficient of variation of K_I values appreciably. This is because by increasing the void content (which replaces particles and matrix in the FGM microstructure), no substantial change is made in the total variability due to the location characteristics of the constituents (in terms of particle and void locations). Furthermore, the particle gradation parameter (cases 7 and 8) also has a noticeable effect on the K_I statistics. For case 7, the mean value of K_I increases from that for case 1. This can be explained by the following facts. As the overall particle content for case 7 ($n_p = 0.5$) is much higher than that for case 1 ($n_p = 1$), it lowers the individual K_I values for case 7. At the same time, due to the higher value of ϕ_p at the crack-tip location for case 7, more samples contain particle at the crack tip. The K_I value for an FGM sample containing particle at the crack tip is much higher than that for a sample containing matrix at the crack tip. Therefore, the mean of K_I for case 7 is higher than that for case 1. A similar argument explains why the mean of K_I for case 8 ($n_p = 2$), which has a significantly lower value of ϕ_p at the crack-tip location compared with case 1, is lower than that for case 1. Since case 7 contains a greater number of particles and particles are fully penetrable, individual particles coalesce to form larger particle clusters and in the process lose their individual location characteristics, thereby reducing the variability of K_I .

Results for the means and coefficients of variation of K_{II} for cases 1–4 shows a similar trend as that observed for K_I . Therefore, from the results of both K_I and K_{II} , it can be concluded that statistical properties of SIFs do not alter appreciably due to particle shape and orientation. By introducing porosity (cases 5 and 6), the mean values of K_{II} change appreciably, as can be observed by a 29.7% increase in the value for case 5 compared with case 1. Variability in the K_{II} values also increases substantially due to the presence of voids. Although the total variability due to location characteristics of the constituents remains comparable even with an increase in the void content, K_{II} is more dependent on the variability in void locations, which increases with the increase in porosity. Hence, results for both K_I and K_{II} indicate that the amount of porosity substantially enhances crack-driving forces. Results for

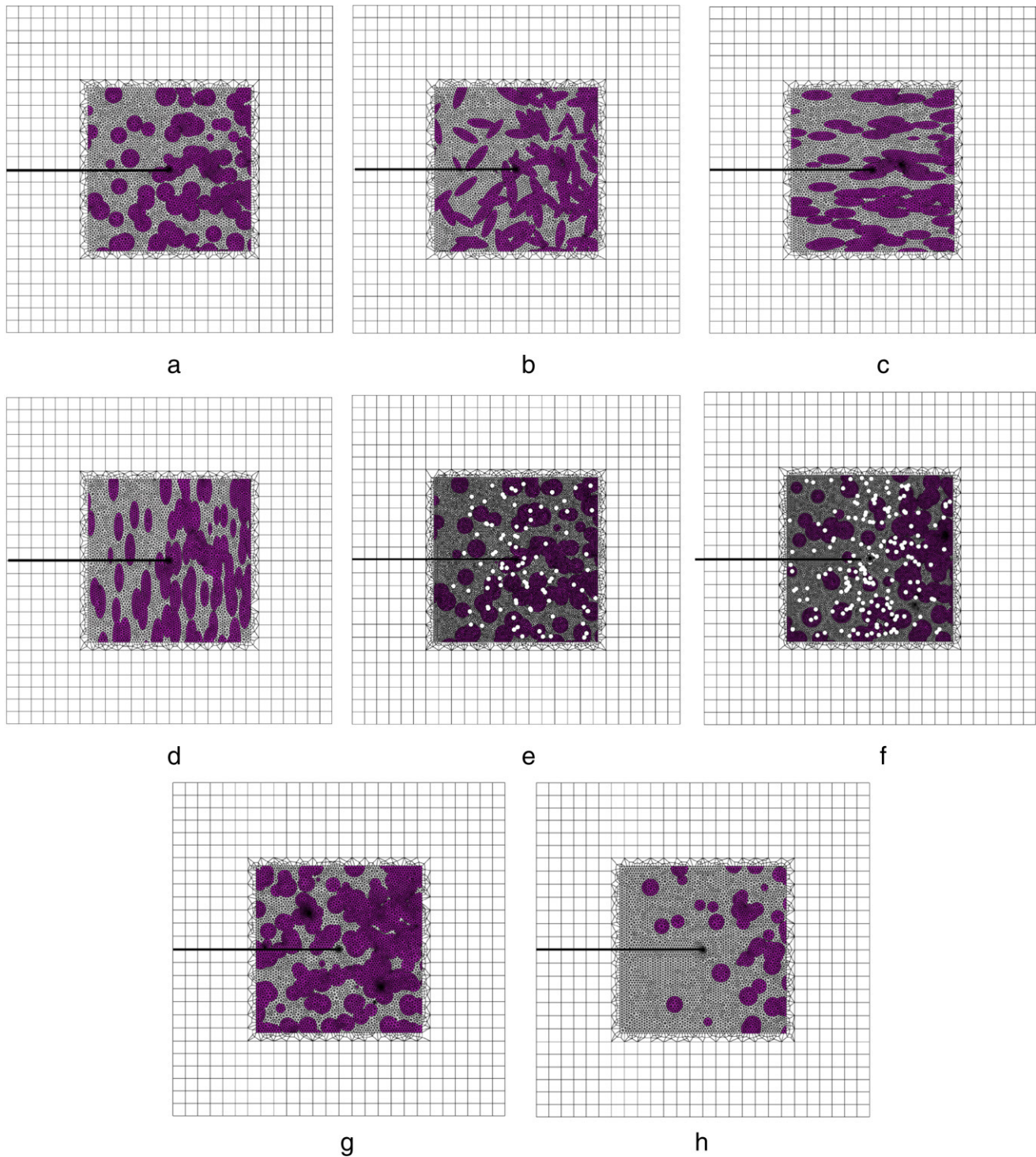


Fig. 6. Finite-element discretizations for sample FGM specimens employing concurrent multiscale model: (a) case 1; (b) case 2; (c) case 3; (d) case 4; (e) case 5; (f) case 6; (g) case 7; (h) case 8.

the means and coefficients of variation of K_{II} for cases 7 and 8 show a similar trend as that observed for K_I , which indicates that particle gradation parameter also has a noticeable impact on the SIF statistics.

4.4.2. Fracture reliability

While the second moment statistics are useful, a more meaningful stochastic response is the conditional probability of fracture initiation, $P_F(K_{Ic}) := P[\gamma(\mathbf{R}) < 0]$, described in Section 2.3. The failure probability $P_F(K_{Ic})$ derived from the maximum

circumferential stress theory was calculated by the concurrent multiscale model for different FGM microstructures. Fig. 8(a) plots how $P_F(K_{Ic})$ varies as a function of the fracture toughness K_{Ic} for non-porous FGMs with different microstructures containing circular and elliptical particles with different orientations, all generated using $n_p = 1$ (cases 1, 2, 3, and 4). The results indicate that the effects of particle shape and orientation on fracture reliability are small. This can be attributed to the following reason. Due to the fully penetrable particle model, particles of different shapes and orientations coalesce to achieve a target volume fraction and

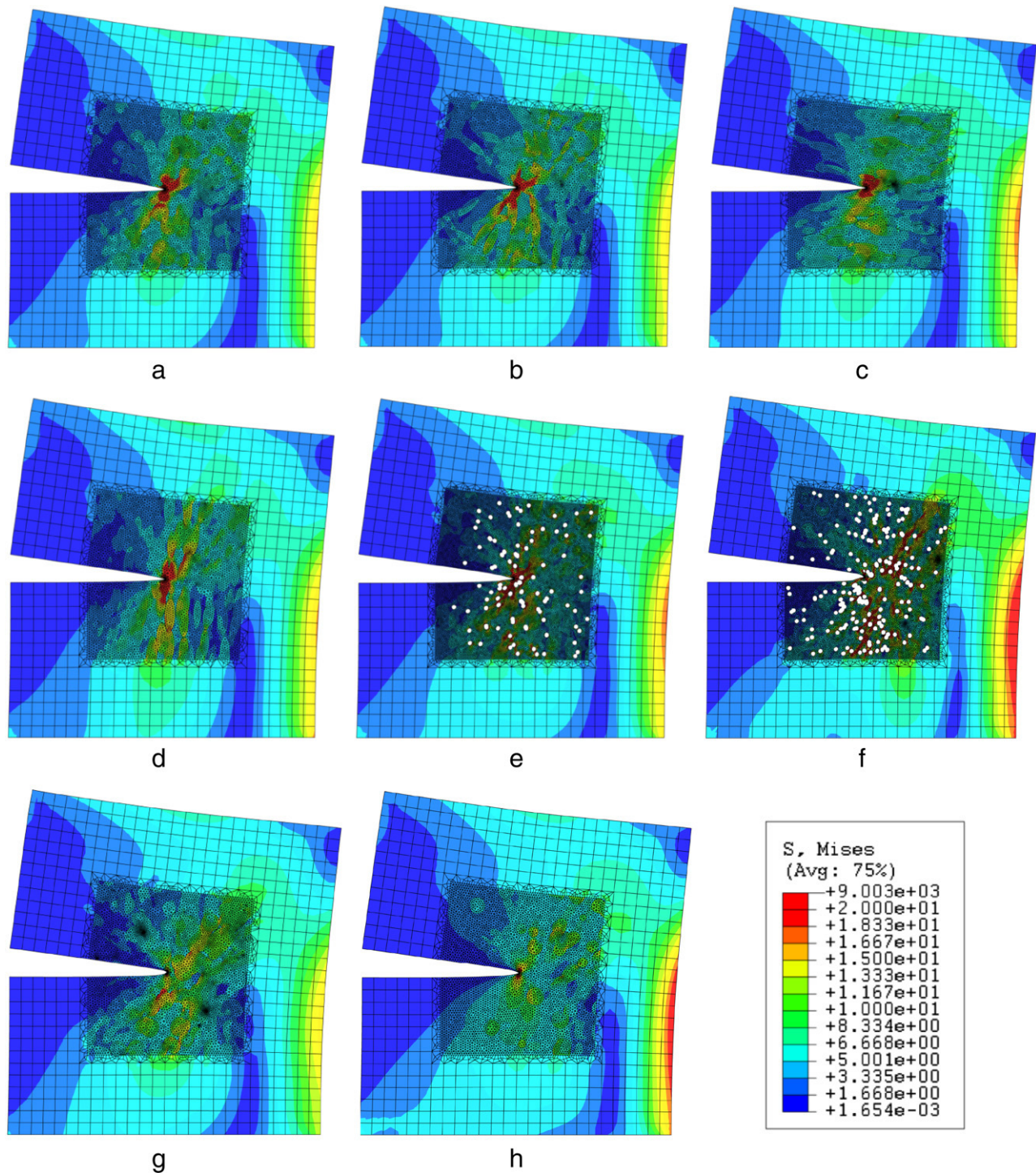


Fig. 7. von Mises stress contours for sample specimens of SiC–Al FGM employing concurrent multiscale model: (a) case 1; (b) case 2; (c) case 3; (d) case 4; (e) case 5; (f) case 6; (g) case 7; (h) case 8.

therefore lose their geometric identities, except at very low volume fractions. In the present study, ϕ_p is close to 0.5 near the crack tip. Therefore, close to the crack tip, overall particle domains are similar for different particle shapes and orientations. Since SIFs are strongly influenced by the particles near the crack tip, effects of particle shape and orientation on fracture reliability are negligible. Also, due to the bi-axial nature of stresses surrounding the crack tip, particle orientation has little or no contribution in shielding the crack tip from applied loads and therefore has negligible effect on SIFs, and hence on fracture reliability.

To further investigate the effect of particle orientation, an additional analysis was performed using a very high stiffness ratio between particle and matrix. For the SiC–Al FGM, the ratio of the mean value of elastic modulus of SiC to that of Al, defined as the modular ratio, is $419.2/69.7 \approx 6.0$. A new FGM, made of SiC as particles and Polyimide as the matrix, was considered, which has a modular ratio of 40. Statistical properties of the elastic moduli E_{SiC} and $E_{\text{Polyimide}}$ and the Poisson's ratios ν_{SiC} and $\nu_{\text{Polyimide}}$, of SiC and Polyimide, respectively, are listed in Table 6. The motivation for choosing samples of FGM with a very high modular ratio

Table 4
Numbers and types of finite elements for various FGM microstructures.

Case	No. and type of elements ^a in $\mathcal{D} \setminus \overline{\mathcal{D}}$	No. and type of elements ^a in $\overline{\mathcal{D}} \setminus \mathcal{D}_\epsilon$	No. and type of elements ^a in \mathcal{D}_ϵ
1	818 Type-1 160 Type-2	10,302 Type-2	168 Type-1 12 Type-3
2	835 Type-1 149 Type-2	10,249 Type-2	168 Type-1 12 Type-3
3	832 Type-1 139 Type-2	10,485 Type-2	168 Type-1 12 Type-3
4	840 Type-1 152 Type-2	10,222 Type-2	168 Type-1 12 Type-3
5	1093 Type-1 213 Type-2	21,302 Type-2	168 Type-1 12 Type-3
6	1052 Type-1 222 Type-2	20,497 Type-2	168 Type-1 12 Type-3
7	816 Type-1 168 Type-2	11,120 Type-2	168 Type-1 12 Type-3
8	822 Type-1 132 Type-2	9802 Type-2	168 Type-1 12 Type-3

^a Type-1: eight-noded, non-singular, quadrilateral elements. Type-2: six-noded, non-singular, triangular elements. Type-3: eight-noded, quarter-point (singular), collapsed quadrilateral elements.

Table 5
Second-moment statistics of SIFs.

Case	K_I (MPa \sqrt{m})		K_{II} (MPa \sqrt{m})	
	Mean	Coefficient of variation (%)	Mean	Coefficient of variation (%)
1	25.170	44.736	2.070	98.599
2	25.237	45.192	2.085	95.779
3	26.052	43.095	2.096	90.410
4	24.780	46.029	2.038	84.593
5	26.069	43.654	2.684	141.095
6	29.588	45.451	2.678	183.308
7	26.462	37.291	2.379	82.682
8	23.955	44.254	1.970	86.345

Table 6
Statistical properties of constituents in SiC–Polyimide FGM.

Elastic property ^a	Mean	Coefficient of variation (%)	Probability distribution
E_{SiC} (GPa)	419.2	15	Lognormal
$E_{Polyimide}$ (GPa)	10.48 ^b	10	Lognormal
ν_{SiC}	0.19	15	Lognormal
$\nu_{Polyimide}$	0.34	10	Lognormal

^a $E_p = E_{SiC}; E_m = E_{Polyimide}; \nu_p = \nu_{SiC}; \nu_m = \nu_{Polyimide}$.

^b 419.2/40.

is that the orientation of particles will strongly influence the effective orthotropic material properties of an FGM with high elastic mismatch. Therefore, the effect of particle orientation on FGM fracture, if any, can be enhanced. However, fracture reliability results of SiC–Polyimide FGM depicted in Fig. 8(b) show no statistically significant differences among the failure probability curves with circular and elliptical particles entailing different orientations. Hence, it can be concluded that due to the fully penetrable particles and biaxial nature of stresses around the crack tip, particle shape and orientation have negligible effects on fracture reliability, even for FGMs with a very high modular ratio.

Fig. 9 plots the variation of $P_F(K_{Ic})$ as a function of the fracture toughness K_{Ic} for porous FGMs with different void contents (cases 5 and 6). All porous microstructures contain circular particles generated using $n_p = 1$. From Fig. 9, porosity has a significant effect on fracture reliability. Compared with the non-porous FGM microstructure, the presence of voids increases the probability of fracture initiation. The greater the void content, the greater the probability of fracture initiation, as can be observed from the results of two types of porous FGMs. Since porosity decreases the load-carrying capacity of a structure, more load is transferred to the crack tip, which then becomes more likely to propagate.

Fig. 10 plots how $P_F(K_{Ic})$ varies as a function of the fracture toughness K_{Ic} for non-porous FGMs with microstructures containing circular particles generated using three different values of the particle gradation parameter n_p : 0.5 (case 7), 1 (case 1), and 2 (case 8). From the comparison between Figs(c) and 10, the greater the volume fraction of particles close to the crack tip (obtained by decreasing n_p), the less the probability of failure. Since an increase in particle content close to the crack tip shields the crack from applied external loads more effectively, the crack in an FGM with a higher particle volume fraction at the crack-tip region has a lower propensity to propagate.

4.4.3. Crack propagation

A limited crack-propagation simulation was conducted to evaluate the effect of material fracture toughness of a non-porous FGM. The microstructure contains circular particles ($\sigma_1 = \sigma_2 = \sqrt{0.3 \times 0.1}$ cm) and the particle gradation parameter $n_p = 1$ (cases 9, 10, and 11). Crack trajectories were determined based on the maximum circumferential stress theory with an incremental crack length of $\Delta a_c = 0.5$ cm. Since particles and matrix are perfectly bonded, a crack can propagate from matrix to particle without changing direction. The initial crack tip is located at $\mathbf{x}_{tip} = \{x_{tip,1}, x_{tip,2}\}^T = \{5, 5\}^T$ cm. The applied external loads were kept constant during the crack propagation, and crack propagation was stopped when $K_{eff}(\mathbf{R}) < K_{Ic}(\mathbf{x}_{tip})$, where $K_{Ic}(\mathbf{x}_{tip})$ is the mode-I material fracture toughness at the crack tip, i.e., $K_{Ic}(\mathbf{x}_{tip}) = K_{Ic,Al}$ if $\mathbf{x}_{tip} \in \mathcal{D}_m$ and $K_{Ic}(\mathbf{x}_{tip}) = K_{Ic,SiC}$ if $\mathbf{x}_{tip} \in \mathcal{D}_p$. Due to random microstructures, crack-propagation analyses were performed for three independent samples.

Fig. 11(a) shows crack propagation paths in three samples when $K_{Ic,Al} = 20$ MPa \sqrt{m} (case 9). Due to low toughness, cracks in all three samples of Fig. 11(a) propagated all the way through the plate. When the toughness of Al was doubled, as in case 10 ($K_{Ic,Al} = 40$ MPa \sqrt{m}) – the results of which are displayed in

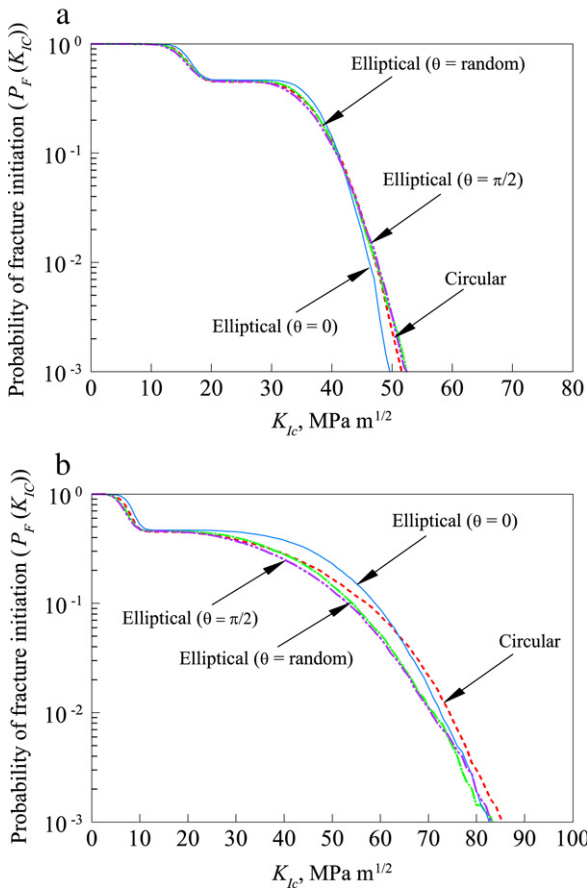


Fig. 8. Probability of fracture initiations of non-porous FGMs with different particle shapes and orientations: (a) SiC–Al FGM; (b) SiC–Polyimide FGM.

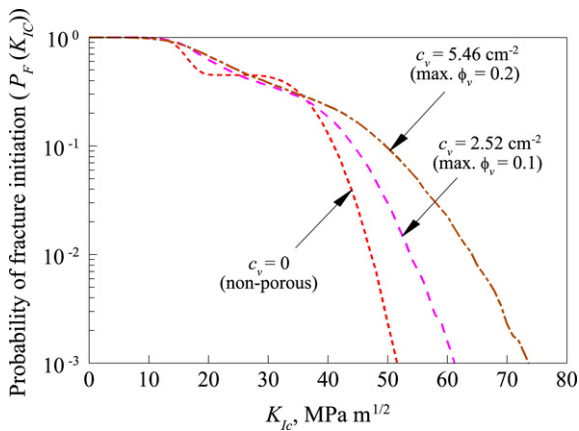


Fig. 9. Probability of fracture initiations of SiC–Al FGMs with different porosities.

Fig. 11(b) – cracks in two of the three samples did not propagate at all. For the remaining sample, the crack was arrested after a single increment. Finally, Fig. 11(c) exhibits crack propagation paths when $K_{Ic,Al} = 30 \text{ MPa}\sqrt{\text{m}}$ (case 11). From Fig. 11(c), a crack in only one sample propagated all the way through the plate, but for the remaining two samples, they were arrested after only a few increments. From the above simulation results, it appears that the fracture toughness of the crack-tip material can have a significant effect on the likelihood of crack-propagation or the extent to which a crack can propagate before being arrested by the crack-tip material.

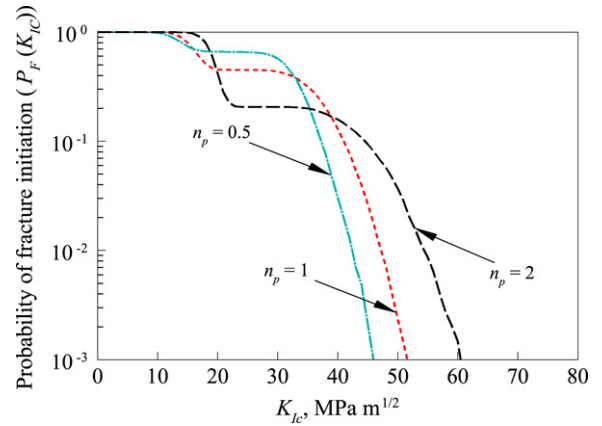


Fig. 10. Probability of fracture initiations of SiC–Al non-porous FGMs with different gradations of intensity functions.

4.5. Computational cost

For a complete stochastic fracture analysis of a given random FGM microstructure, Monte Carlo simulation entailing 10,000 samples were conducted. Therefore, 10,000 deterministic finite-element analyses were involved, leading to a conditional failure probability curve in Figs. 8–10. The underlying deterministic analyses were performed using the concurrent multiscale model and an HP XW8400 workstation. The absolute CPU time required by a single, deterministic multiscale analysis, including all pre-processing efforts, was 50 s. This leads to a full stochastic analysis time of approximately 5.8 days. Therefore, a more efficient but sufficiently accurate stochastic method, if it can be developed, will reduce the computational burden. The need for a computationally efficient stochastic method becomes critical when analyzing three-dimensional FGMs, which are not included in the present study.

5. Conclusions and future work

A parametric study on fracture behavior of a crack in two-dimensional, functionally graded composites was conducted. The study involves stochastic descriptions of particle and void numbers; location, size, and orientation characteristics; and constituent elastic properties; a concurrent multiscale model for determining crack-driving forces under mixed-mode loading; and Monte Carlo simulation for uncertainty propagation and fracture reliability analysis. A level-cut, inhomogeneous, filtered Poisson field describes the statistically inhomogeneous random microstructure of a non-porous or porous, graded composite. The concurrent multiscale model involves simultaneously performed microscale and macroscale analyses.

A numerical problem involving an edge-cracked, functionally graded specimen under a mixed-mode deformation was analyzed to calculate the statistical moments of crack-driving forces, the conditional probability of fracture initiation, and sample properties of crack-propagation. Eight distinct varieties of graded microstructure encompassing circular and elliptical particles; deterministic and random particle orientations; low and high porosity contents; and low, medium, and high particle gradation parameters, were analyzed. In addition, three distinct values (low, medium, and high) of fracture toughness properties of the matrix material were examined. The results pertaining to a stationary crack demonstrates that (1) particle shape and orientation for the same phase volume fractions have negligible effects on fracture reliability, even for graded media with a high modular ratio; (2) voids strongly influence crack-driving forces by rendering the graded microstructure weaker, thereby significantly

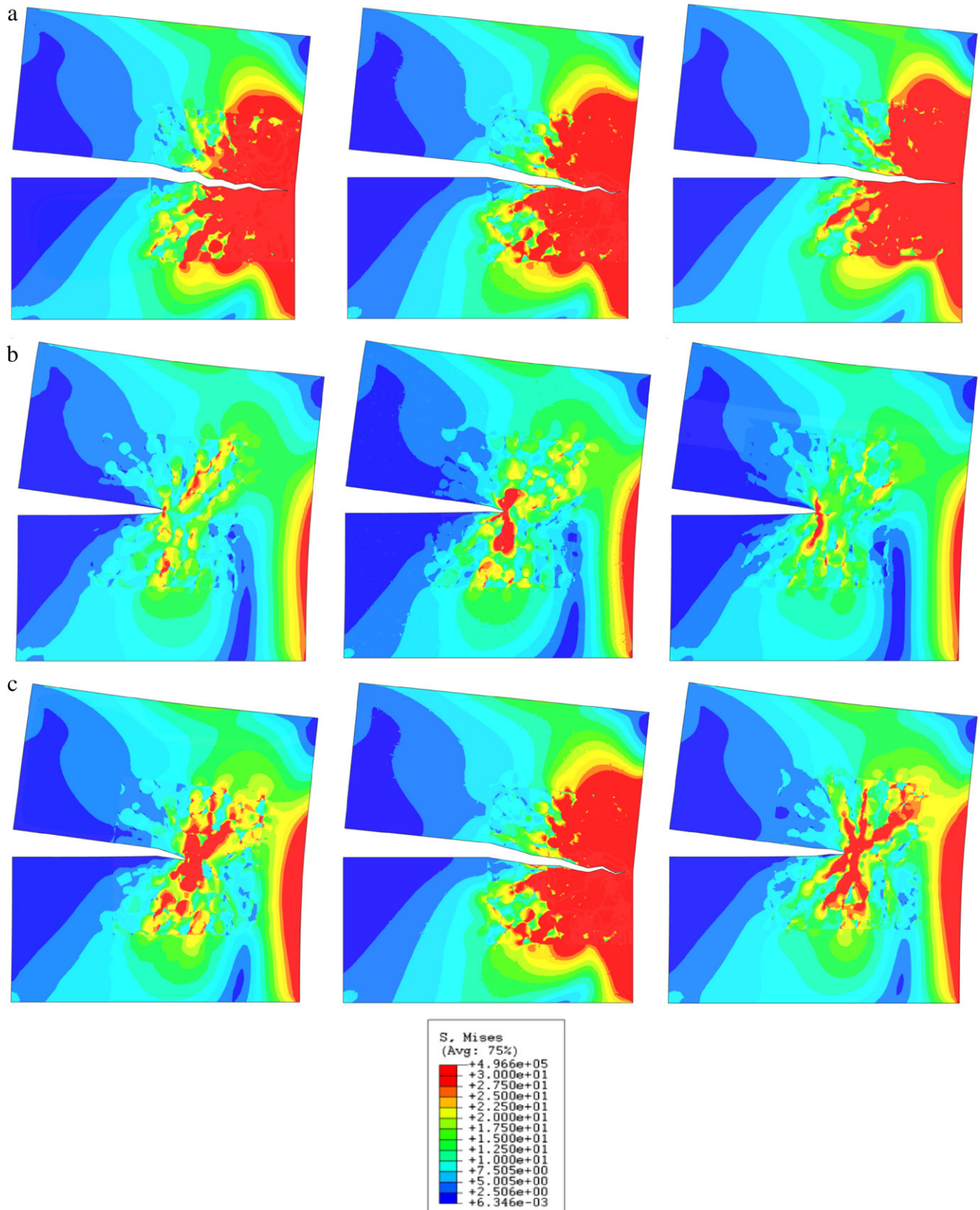


Fig. 11. Crack paths for SiC–Al FGM samples with different $K_{Ic,Al}$: (a) $K_{Ic,Al} = 20 \text{ MPa}\sqrt{\text{m}}$; (b) $K_{Ic,Al} = 40 \text{ MPa}\sqrt{\text{m}}$; (c) $K_{Ic,Al} = 30 \text{ MPa}\sqrt{\text{m}}$.

raising the probability of fracture initiation; and (3) increasing the particle gradation parameter, which is inversely related to particle volume fraction, significantly increases the probability

of fracture initiation. The crack propagation results for perfectly bonded composites with brittle particles reveal that under a fixed external loading, the fracture toughness of the matrix material can

have a significant effect on the likelihood or the extent of crack growth.

The stochastic analysis conducted using Monte Carlo simulation requires a large number of deterministic finite-element analyses. Further research is necessary to develop alternative stochastic methods that are sufficiently accurate but generate probabilistic solutions in a computationally efficient way.

Acknowledgments

The authors would like to acknowledge financial support from the US National Science Foundation under Grant No. CMS-0409463.

References

- [1] Suresh S, Mortensen A. Fundamentals of functionally graded materials. London: Institute of Materials; 1998.
- [2] Miyamoto Y, Kaysser WA, et al. Functionally graded materials: Design, processing and applications. Boston: Kluwer Academic Publishers; 1999.
- [3] Rao BN, Rahman S. Meshfree analysis of cracks in isotropic functionally graded materials. *Engineering Fracture Mechanics* 2003;70(1):1–27.
- [4] Dolbow JE, Gosz M. On the computation of mixed-mode stress intensity factors in functionally graded materials. *International Journal of Solids and Structures* 2002;39(9):2557–74.
- [5] Kim JH, Paulino GH. Finite element evaluation of mixed-mode stress intensity factors in functionally graded materials. *International Journal for Numerical Methods in Engineering* 2002;53(8):1903–35.
- [6] Rao BN, Rahman S. An interaction integral method for analysis of cracks in orthotropic functionally graded materials. *Computational Mechanics* 2003;32:40–51.
- [7] Mura T. *Micromechanics of defects in solids*. 2nd revised ed. Dordrecht (The Netherlands): Kluwer Academic Publishers; 1991.
- [8] Nemat-Nasser S, Hori M. *Micromechanics: Overall properties of heterogeneous materials*. 2nd ed. Amsterdam (The Netherlands): North-Holland; 1999.
- [9] Grigoriu M. Random field models for two-phase microstructures. *Journal of Applied Physics* 2003;94(6):3762–70.
- [10] Rahman S. A random field model for generating synthetic microstructures of functionally graded materials. *International Journal for Numerical Methods in Engineering* 2008;76(7):972–93.
- [11] Ferrante FJ, Graham-Brady LL. Stochastic simulation of non-gaussian/non-stationary properties in a functionally graded plate. *Computer Methods in Applied Mechanics and Engineering* 2005;194:1675–92.
- [12] Graham-Brady LL, Xu XF. Stochastic morphological modeling of random multiphase materials. *Journal of Applied Mechanics* 2008;75(6):061001.
- [13] Chakraborty A, Rahman S. Stochastic multiscale models for fracture analysis of functionally graded materials. *Engineering Fracture Mechanics* 2008;75:2062–86.
- [14] Rahman S, Chakraborty A. A stochastic micromechanical model for elastic properties of functionally graded materials. *Mechanics of Materials* 2007;39:548–63.
- [15] Anderson TL. *Fracture mechanics—Fundamentals and applications*. 2nd ed. Boca Raton (Florida): CRC Press; 1995.
- [16] Rubinstein RY. *Simulation and the Monte Carlo method*. New York (NY): John Wiley & Sons; 1981.
- [17] ABAQUS 6.7. *User's guide and theoretical manual, version 6.7*. Providence (RI): ABAQUS Inc; 2007.
- [18] Tandon GP, Weng GJ. The effect of aspect ratio of inclusions on the elastic properties of unidirectionally aligned composites. *Polymer Composites* 1984;5(4):327–33.